Sakarya University Journal of Science

ISSN : 2147-835X
Publisher : Sakarya University

Vol. 28, No. 6, 1285-1295, 2024
DOI: https://doi.org/10.16984/saufenbilder.1381531

Research Article

Optical and Morphology Mechanism of CeO_2 Thin Films Prepared by Ultrasonic Spray Pyrolysis Method

Murat Kellegöz[1*], Sema Kurtaran[1]

[1] Eskisehir Osmangazi University, Faculty of Science, Department of Physics, Eskisehir, Türkiye, murke@ogu.edu.tr, skurtaran@ogu.edu.tr
[*]Corresponding Author

ARTICLE INFO

Keywords:
CeO_2 thin films
Ultrasonic spray pyrolysis method
Material characterisations

Article History:
Received: 27.10.2023
Accepted: 14.12.2024
Online Available: 20.12.2024

ABSTRACT

Cerium oxide (CeO_2) thin films were successfully fabricated on glass substrates via spray pyrolysis at 350°C with varying molarities (0.025, 0.05 and 0.1 M). We employed various characterisation techniques to assess how molarity influences these thin films' microstructural, optical, morphological, and surface properties. The as-synthesized samples exhibited a distinct face-centred cubic fluorite structure oriented along the (2 0 0) crystallographic plane. Raman spectroscopy provided insights into imperfections, with the longitudinal optical mode confirming the presence of oxygen vacancies. The peak asymmetry and width in the Raman spectra were associated with the existence of Ce^{+3} ions and oxygen vacancies. Photoluminescence spectra (PL) illustrated an excitation peak at 400 nm and two emission peaks at 525 nm and 600 nm. Our scanning electron microscopy (SEM) images illustrated how molarity affected the morphologies of the samples, while atomic force microscopy (AFM) allowed us to investigate the film's surface morphologies and roughness values. Transmittance analysis within UV-Vis spectral range indicated that these samples were transparent, with transmittance levels ranging from 20% to 60%. Furthermore, we observed a decrease in the band gap energy (E_g) with increasing molarity. These findings hold significant promise for expanding the applications of cerium oxide in technological devices.

1. Introduction

Metal oxide thin films have applications in different technological fields [1]. Cerium oxide (CeO_2) stands out among the different types of metal oxide thin films due to its remarkable material properties. It is highly suitable for different applications, such as fuel cells and sensors [2-4]. Cerium (Ce) is a chemical element with atomic number 58 and belongs to the lanthanide series of elements. It has a standard atomic weight of 140.116 g/mol and is known for its exceptional reactivity and versatility in various chemical and technological applications [5].

The CeO_2, or ceria, is a binary compound composed of cerium and oxygen. It exhibits a fluorite crystal structure and unique redox properties, making it an important material for numerous industrial and scientific applications [6].

In recent years, CeO_2 thin films have garnered significant attention in various technological fields due to their remarkable properties, which include high oxygen storage capacity, excellent catalytic activity, superior optical absorption and transparency, exceptional chemical stability, and superior electrical conductivity. These films have shown great potential in electronic and optoelectronic applications, as their unique combination of optical, electrical, and mechanical properties enables their versatile utilization as protective coatings, transparent

Cite as: M. Kellegöz, S. Kurtaran (2024). Optical and Morphology Mechanism of CeO2 Thin Films Prepared by Ultrasonic Spray Pyrolysis Method, *Sakarya University Journal of Science*, 28(6), 1285-1295. https://doi.org/10.16984/saufenbilder.1381531

conductive layers, and dielectric materials [7-10].

The unique properties of the CeO_2 thin films make them highly promising for utilization in gas sensors, solid oxide fuel cells, and protective coatings. Their ability to store and release oxygen efficiently contributes to enhanced catalytic performance and fuel cell efficiency [3, 7, 8, 11]. Additionally, the distinctive properties of CeO_2 make them ideal candidates for catalytic applications. Due to their oxygen vacancy defects and redox behaviours, they can act as effective catalysts for various reactions, including oxidation, hydrogenation, and pollutant degradation [12, 13].

There are many techniques for fabricating the CeO2 films, samples, nanostructures, etc., such as chemical precipitation [14, 15], sol-gel synthesis [16, 17], thermal decomposition [18, 19], hydrothermal synthesis [20, 21], microwave-assisted synthesis [22], electrodeposition [23], and spray pyrolysis [24]. These methods offer control over the particle size, morphology, and properties of the resulting CeO_2 materials.

Spray pyrolysis is a versatile and efficient technique that offers numerous advantages in materials synthesis and deposition. One key advantage is its scalability and cost-effectiveness, allowing for large-scale production with minimal equipment requirements and utilizing low-cost precursors [25]. Additionally, spray pyrolysis enables precise control over film thickness and composition by adjusting precursor concentration, spray parameters, and thermal conditions [26]. The technique also allows for uniform and conformal coatings deposition on complex-shaped substrates, making it suitable for various applications such as energy storage devices, catalysis, and photovoltaics [27].

Furthermore, spray pyrolysis facilitates the synthesis of multi-component materials and the incorporation of dopants, leading to enhanced properties and tailored functionalities [28]. Lastly, this technique provides versatility in terms of the types of materials that can be created, including metal oxides, semiconductors, and nanomaterials [29]. While spray pyrolysis is a versatile technique with numerous advantages, it also has certain disadvantages that should be considered. One limitation of spray pyrolysis is the potential for forming non-uniform coatings resulting from uneven droplet distribution or non-homogeneous precursor decomposition [25]. Furthermore, the control of film morphology, particularly in grain size and orientation, can be challenging, leading to variations in film properties [26].

Another drawback is the limited scalability of the technique for some materials, as certain precursors may exhibit poor solubility or stability in the solution, hindering the uniform deposition of high-quality films [27]. Additionally, the reliance on high temperatures during pyrolysis can impose constraints on the choice of substrate materials, limiting the range of compatible substrates for the deposition process [28]. Lastly, the deposition rate in spray pyrolysis can be relatively slow compared to other deposition techniques, which may be a concern for high-throughput applications [29].

In this study, we present a comprehensive investigation of the chemical deposition of CeO_2 by a chemical pyrolysis technique. We aim to elucidate the fundamental aspects of this synthesis route and provide valuable insights into the process parameters, reaction mechanisms, and material characteristics. Through systematic experiments and characterization techniques, we seek to uncover the relationships between the deposition conditions, microstructure, chemical composition, and functional properties of the resulting CeO_2 films.

The manuscript is harmonized as follows: Firstly, we provide a detailed overview of the chemical pyrolysis technique, including its principles, advantages/disadvantages, and previous applications in synthesising various materials. Next, we describe the experimental methodology employed in this study, encompassing the selection of precursors, deposition conditions, and characterization techniques. Subsequently, we present the results and discussion section, where we analyze the influence of different process parameters on the deposition efficiency, crystallinity, morphology, and chemical

composition of the CeO_2 films. Finally, we summarise our findings, their implications for future research, and potential applications of the synthesized CeO_2 materials.

2. Materials and Methods

In this research, we employed the ultrasonic spray pyrolysis (USP) method to create thin films of CeO_2. The process involved depositing these thin films on glass substrates using cerium (III) nitrate hexahydrate [$Ce(NO_3)_3.6H_2O$] as the source material. Initially, we prepared precursors in deionised water at concentrations of 0.025, 0.05, and 0.1 M. We sprayed 100 cc of the prepared solution onto glass substrates for approximately 10 minutes using an ultrasonic nozzle. The detailed synthesis procedure can be found in a prior study [30, 31]. We employed compressed air as the propellant to atomise and deliver the solution onto the target substrate while concurrently regulating the surface temperature at 350±5°C.

The flow rate of the solution was controlled at 5 cm^3min^{-1} using a flowmeter and the nozzle. The glass substrate was positioned about 30 cm asunder. The resulting CeO_2 thin films were labelled C1, C2, and C3, corresponding to molarities of 0.025, 0.05, and 0.1 M, respectively. We examined the structural characteristics of these films using CuKα radiation (λ = 1.5406 Å) with an X-ray diffractometer (XRD). Additionally, an emission scanning electron microscope (SEM) was utilized to assess the morphological properties of the films (specifically, a Hitachi Regulus 8230 model). We used a UV- Vis spectrophotometer to determine the films' absorbance spectra in the 300 to 900 nm range (Shimadzu-Solid 2550). Investigating deposited thin films through optical analysis involved utilising Photoluminescence (PL) techniques employing a PerkinElmer LS55 spectrometer. The spectrometer employed a xenon arc lamp as the light source, emitting at a wavelength of 325 nm. Surface images and roughness were captured using a Park Systems XE-100 atomic force microscope (AFM), while Raman spectra were recorded using Renishaw's Via Raman microscope. The films' thickness was measured using a coating thickness gauge (Elcometer 345 Instrument). The average C1, C2 and C3 thicknesses were 140, 200 and 360 nm, respectively.

3. Results and Discussion

3.1. Crystal structure analysis

The XRD apparatus pivots in examining crystal structures, dimensions, and morphologies and identifying unintended phases within the material's arrangement. Figure 1 exhibits the diffraction patterns of films fabricated via the USP technique. The XRD equipment is a critical characterization instrument for ascertaining crystal structures, dimensions, and shapes and identifying any undesirable phases in the material. It illustrates the diffraction patterns of films generated through the USP process.

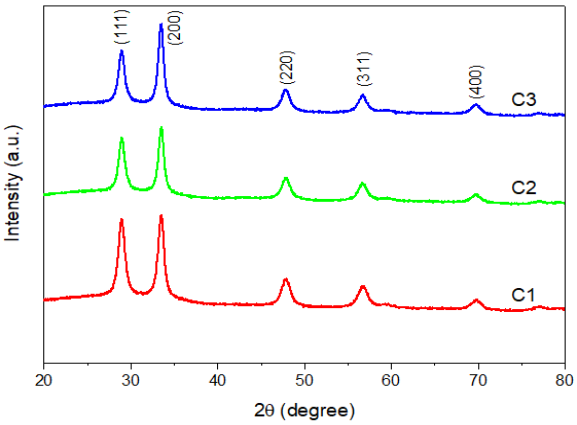

Figure 1. CeO_2 thin films' XRD diffraction pattern

Table 1. CeO_2 thin films' XRD data

Film	2θ (°)	d (Å)	$2\theta_0$ (°) (ASTM)	d_0 (Å) (ASTM)	(hkl)
C1	29.06	3.073	28.01	3.183	(1 1 1)
	33.46	2.676	32.45	2.757	(2 0 0)
	47.70	1.905	46.55	1.949	(2 2 0)
	56.61	1.625	55.21	1.662	(3 1 1)
	69.87	1.345	67.96	1.378	(4 0 0)
C2	28.88	3.092	28.01	3.183	(1 1 1)
	33.60	2.667	32.45	2.757	(2 0 0)
	48.01	1.895	46.55	1.949	(2 2 0)
	56.68	1.624	55.21	1.662	(3 1 1)
	69.79	1.348	67.96	1.378	(4 0 0)
C3	28.94	3.086	28.01	3.183	(1 1 1)
	33.41	2.682	32.45	2.757	(2 0 0)
	47.83	1.902	46.55	1.949	(2 2 0)
	56.90	1.618	55.21	1.662	(3 1 1)
	69.73	1.349	67.96	1.378	(4 0 0)

The powdered nanoparticles' XRD pattern was measured in the 2θ range from 20 to 80 degrees. As seen in Table 1, the XRD pattern revealed prominent peak positions at (111), (200), (220),

(311), and (400) on the 2θ plane axis. These XRD diffraction features were consistent with the cubic structure of CeO_2 and aligned with the reference-coded ASTM (American Society for Testing Materials) card number 98-015-5608.

Apart from peak shifts, alterations were observed in the lattice parameter and crystal dimensions. To calculate the crystal dimensions, we employed the Debye–Scherrer equation [32]:

$$D = \frac{0.89\lambda}{\beta \cos\theta} \quad (1)$$

where D represents the crystallised size, λ is the wavelength of the incident X-ray, β is the full width at half maximum (FWHM) in radians of the diffraction peak, and θ is the Bragg angle.

The findings indicated the absence of peaks associated with impurities. XRD patterns consistently revealed prominent (111) and (200) planes in all the films [33]

The value of macro strain, denoted as <e>, represents the shift in the crystal peak positions and can be determined using the following equation [34].

$$< e >= \frac{d - d_0}{d_0} \quad (2)$$

where d_0 is the interplanar spacing without deformation, and d is the interplanar spacing. The dislocation density (δ) has been utilized to estimate by the following equation [35]

$$\delta = \frac{1}{D^2} \quad (3)$$

Due to stress within the crystal structure, the size reduction occurred in the direction opposite to the unit cell parameter.

The parameters, including D, $<e>$, and δ, are given in Table 2.

Table 2. CeO_2 thin films' structural parameters for (1 1 1) and (2 0 0) plane

Film		β(°)	D(nm)	<e>	δ(1/nm^2) x10^{-3}
C1	(111)	0.230	35.62	-0.035	0.788
	(200)	0.218	38.04	-0.030	0.691
C2	(111)	0.128	64.15	-0.029	0.243
	(200)	0.461	18.05	-0.033	3.069
C3	(111)	0.179	45.82	-0.031	0.476
	(200)	0.435	19.10	-0.032	2.741

The prevalence of (111) and (200) reflections in the fluorite-type face-centered cubic structure highlighted a preference for crystal growth in this specific orientation. The (111) and (200) planes were observed dominantly at all molarities. D of the resulting films ranged from 18 to 64 nm, and the observed increase in β in the film with the smallest grain size suggests a less-than-ideal crystal structure. Low macro stress values indicate minimal deformation in the crystal lattice.

3.2. Raman analysis

While XRD analysis yields extensive data for elucidating crystal properties, it proves insufficient for interpreting alterations induced by oxygen ions. Conversely, Raman spectroscopy findings assume significance in explaining oxygen ion vacancy formation [36, 37]. As depicted in Figure 2, the Raman spectra of films within the 100–1000 cm^{-1} range are presented.

The distinctive spectral feature detected at approximately 465 cm^{-1} corresponds to the F_{2g} Raman-active internal phonon mode. It is consistent with the crystallographic symmetry of the Fm3m space group within the fluorite lattice structure [38-40]. As illustrated in Figure 2, the peak at around 600 cm^{-1} signifies the formation of oxygen vacancies. This oxygen vacancy formation induces pronounced absorption in the ultraviolet (UV) region. The generated vacancy actively contributes to luminescence.

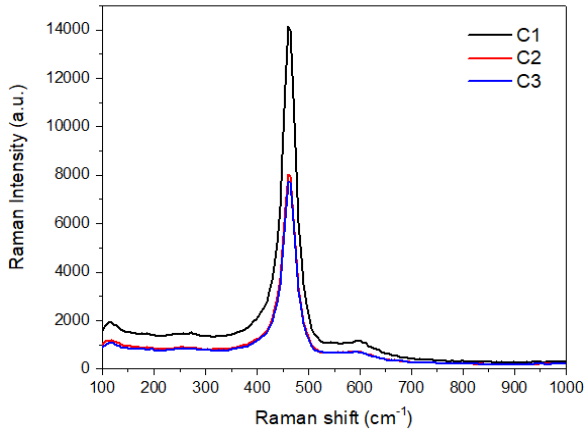

Figure 2. Raman spectra of CeO_2 thin films

3.3. UV-Vis analysis

UV-Vis analysis was used to conduct optical characterization of the CeO_2 thin films. The resultant graphs displaying transmittance and absorbance spectra are presented in Figure 3.

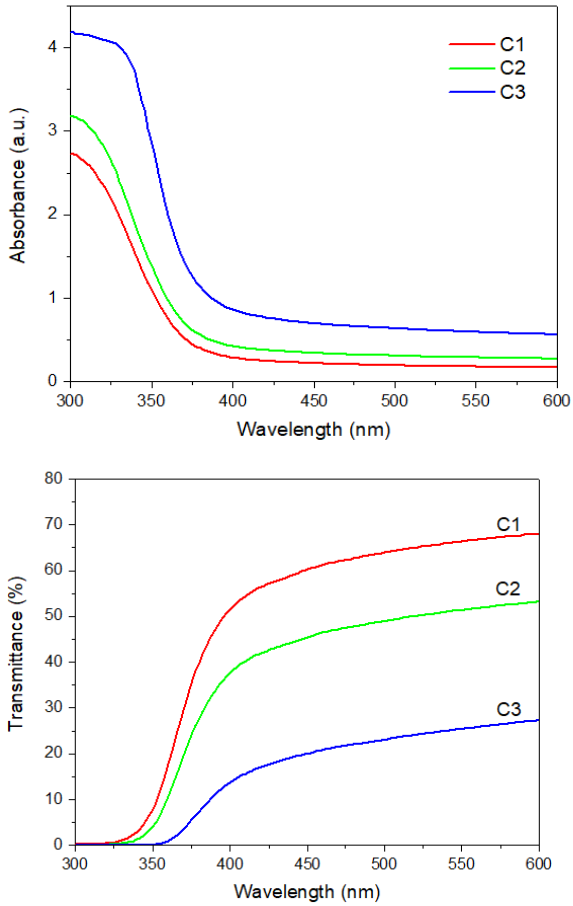

Figure 3. UV–Vis transmittance and absorbance of CeO_2 thin films

In the visible spectrum, the absorbance decreased as a function of increasing wavelength. Upon examination of the transmittance spectra, it was observed that transmittance decreased with increasing molarity. This phenomenon can be attributed to scattering losses occurring within the films' interior and on their surfaces. Consequently, this scattering led to a significant reduction in the films' transparency within the visible region.

The broadening of the fundamental absorption edge in the films also serves as an indicator of heightened deformation near the band edges. Linear absorption coefficients were computed for each film using absorbance spectra based on the expression $\alpha = A/t$. To obtain the optical band gap energy (E_g), graphs depicting $(\alpha h\nu)^2$ as a function of photon energy $h\nu$ for CeO_2 films are presented in Figure 4.

The Tauc relationship was used to directly determine the optical band gap energy of the produced thin films. Figure 4 shows the change of $(\alpha h\upsilon)^2$ with energy $h\upsilon$ for a direct transition using the Tauc formula [29];

$$(\alpha h\upsilon) = A(h\upsilon\text{-}E_g)^n \quad (4)$$

where α absorption coefficient, $h\upsilon$ incident photon energy, A proportionality constant and E_g optical band gap. Since all films have a direct band structure, n was 1⁄2 for the allowed direct transition. Figure 2 shows the optical bandgap values graph.

Figure 4 illustrates the E_g of the CeO_2 thin films, which fall within the 3.38 to 3.51 eV range. The determination of E_g entails the extrapolation of the linear segment of the graph illustrating the relationship between $(\alpha h\nu)^2$ and $h\nu$, as illustrated in Figure 4. Analysis of these graphs reveals that all the films exhibit characteristics of direct band gap materials [41]. The decrease in band gap with an increase in concentration is attributed to the size quantization effect due to the small size of the particles. The absorbance is expected to depend on the oxygen vacancies, optical band gap, impurity centres, defect centres and surface roughness. C1 has small crystallite sizes (35-38 nm), so a higher band gap is expected. C2, with the largest crystallite size (64 nm), probably has the lowest band gap. C3 is medium crystallite, and the band gap is expected between C1 and C2. This study determined that the band gap values

decrease with molarity, consistent with the increase in crystallite sizes. This quality is highly favourable in applications such as photovoltaic solar cells.

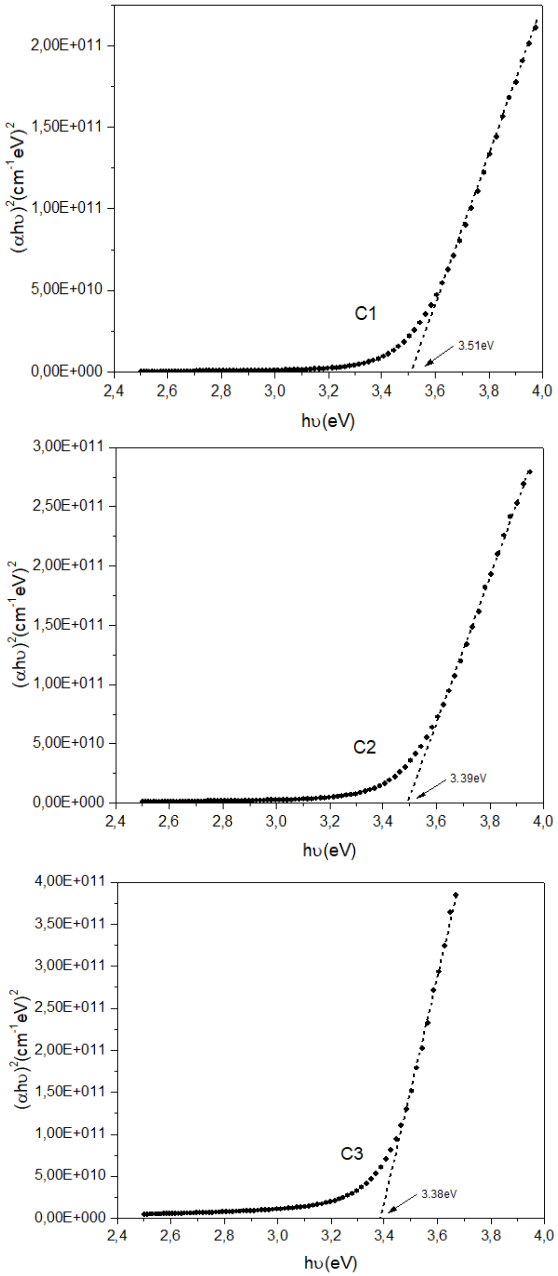

Figure 4. *Eg* of CeO_2 thin films

3.4. The Properties of photoluminescence

In Figure 5, we can observe the excitation and emission spectra of thin films made of CeO_2. This figure shows a prominent excitation peak at 400 nm and two distinct emission peaks at 525 nm and 600 nm in the photoluminescence spectrum of the CeO_2 host crystal when it is in its pure, undoped form. The 400 nm excitation peak arises from the transition originating from the $4f^1$ ground state to the lowest energy level (5d) of Ce^{+3} ions. The crystal field effect splits the 5d energy level of the Ce^{+3} ions, potentially resulting in multiple excitation peaks [42].

Nevertheless, among the potential transitions, the lowest energy transition (4f-5d) is the predominant process within the CeO_2 host crystal. The broad emission spectrum spanning 500 nm to 750 nm, with peak intensities at 525 nm and 600 nm, is attributed to the 5d-4f transition of Ce^{+3} ions. Notably, both the excitation and emission intensities of the host crystal are relatively low.

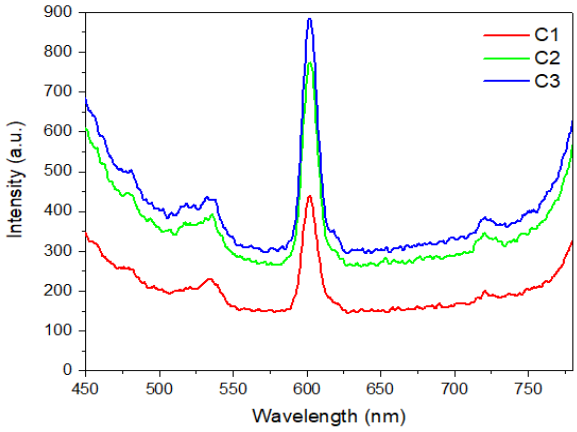

Figure 5. CeO_2 thin films' photoluminescence spectra

3.5. Morphological analysis

Figure 6 provides SEM images of CeO2 thin films. The films' surface morphology highlights variations in grain sizes. Specifically, the analysis reveals that the CeO_2 thin film structure exhibits more excellent uniformity on the surface when coated with a 0.1 M solution than the 0.025 M solution. Furthermore, Figure 6 illustrates the presence of extensive cracking in the films.

This phenomenon arises from the film's contraction during the drying process and the elevated concentration of the precursor solution. The atomic composition, expressed as the percentage of Ce and O elements, has been quantified through EDX analysis and is presented in Table 3.

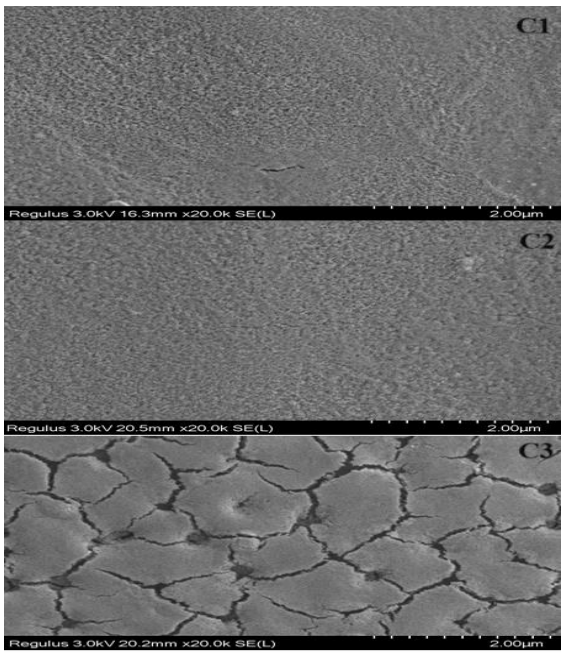

Figure 6. SEM images of CeO_2 thin films'

Table 3. EDX data of CeO_2 thin films

Film	O	Ce	O/Ce
C1	23	77	0.299
C2	36	64	0.563
C3	24	76	0.316

The EDX analysis reveals an augmentation in the Ce/O ratios on the surfaces of the CeO_2 thin films.

3.6. Surface properties

AFM was employed to assess the films' surface topography. Figure 7 depicts 3D representations of CeO_2 thin films captured via AFM.

The films display randomly distributed particle formations of diverse sizes on their surfaces. Furthermore, Table 4 includes the root mean square (R_q) and average (R_a) roughness values of the films.

Table 4. Roughness data of CeO_2 thin films

Film	R_q(nm)	R_a(nm)
C1	8.50	6.29
C2	10.32	6.84
C3	14.49	9.84

Roughness is a pivotal parameter for assessing the optical properties of materials [43]. The roughness values of thin films intended for technological applications hold significant relevance.

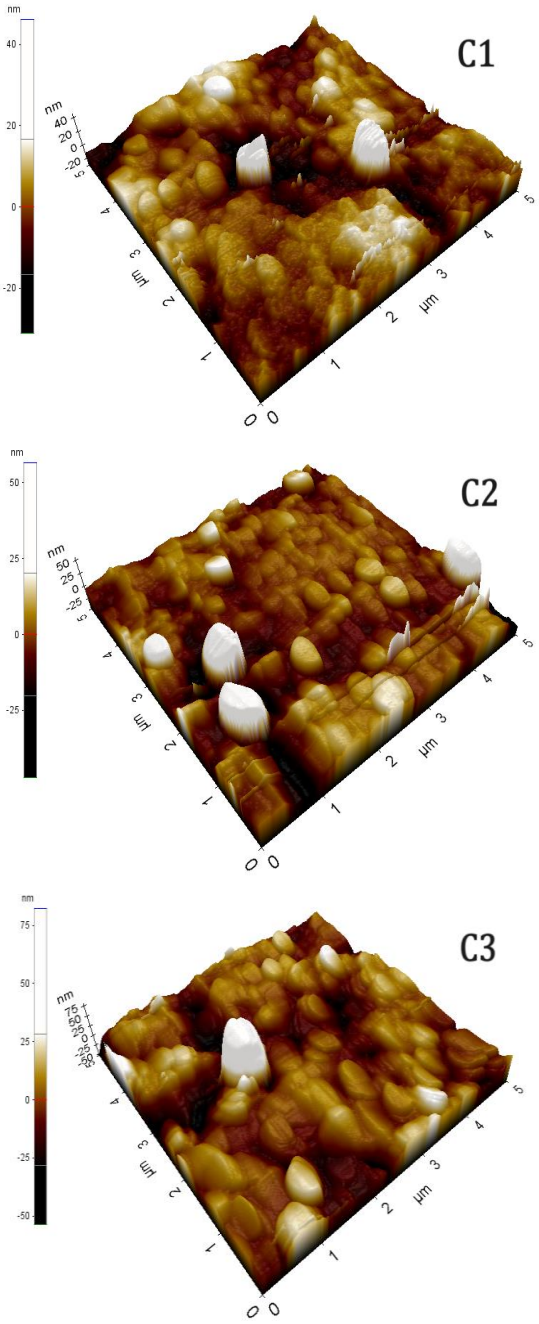

Figure 7. 3D images of CeO_2 thin films

4. Conclusion

In this study, we successfully generated the CeO_2 thin films with varying molarity through spray pyrolysis deposition. XRD measurements conducted on the fabricated CeO_2 thin films revealed a polycrystalline cubic structure, while EDX analyses confirmed their stoichiometric composition. The examined CeO_2 thin films demonstrated a direct energy gap, with the E_g bandgap decreasing from 3.51 to 3.38 eV as molarity varied. The PL and the raman spectroscopy investigations provided evidence that the changes in molarity induced oxygen

vacancies. The PL spectra unveiled the presence of blue emission peaks within the visible spectrum. The primary Raman peak in the CeO_2 thin films occurred at 460 cm^{-1}, corresponding to the F_{2g} vibrational mode. The surface roughness of the films was assessed using AFM, as it is a critical parameter impacting the optical properties of materials. In conclusion, these CeO_2 thin films exhibit promising characteristics for potential applications in optoelectronic devices due to their smooth surface and their high optical conductivity and gas sensors.

Article Information Form

Funding
The author (s) has no received any financial support for the research, authorship or publication of this study.

Authors' Contribution
The authors contributed equally to the study.

The Declaration of Conflict of Interest/ Common Interest
No conflict of interest or common interest has been declared by the authors.

The Declaration of Ethics Committee Approval
This study does not require ethics committee permission or any special permission.

The Declaration of Research and Publication Ethics
The authors of the paper declare that they comply with the scientific, ethical and quotation rules of SAUJS in all processes of the paper and that they do not make any falsification on the data collected. In addition, they declare that Sakarya University Journal of Science and its editorial board have no responsibility for any ethical violations that may be encountered, and that this study has not been evaluated in any academic publication environment other than Sakarya University Journal of Science.

References

[1] N. Tsud, T.Skála, K. Mašek, P. Hanyš, M. Takahashi, H.Suga,T. Mori, H. Yoshikawa, M. Yoshitake, K. Kobayashi, V. Matolín, "Photoemission study of the tin doped cerium oxide thin films prepared by RF magnetron sputtering," Thin Solid Films, vol. 518, no. 8, pp. 2206-2209, 2010.

[2] H. J. Beie, A. Gnörich, "Oxygen gas sensors based on CeO_2 thick and thin films," Sensors and Actuators B: Chemical, vol. 4, no. 3-4, pp. 393-399, 1991.

[3] A. Evans, A. B. Hütter, J. L. M. Rupp, L. J. Gauckler, "Review on microfabricated micro-solid oxide fuel cell membranes," Journal of Power Sources, vol. 194, no. 1, pp. 119-129, 2009.

[4] N. Q. Minh, "Ceramic Fuel Cells," Journal of the American Ceramic Society, vol. 76, no. 3, pp. 563-588, 1993.

[5] K. B. Kusuma, M. Manju, C. R. Ravikumar, N. Raghavendra, M. A. Shilpa Amulya, H. P. Nagaswarupa, H. C. Ananda Murthy, M. R. Anil Kumar, T. R. Shashi Shekhar, "Photocatalytic degradation of Methylene Blue and electrochemical sensing of paracetamol using Cerium oxide nanoparticles synthesized via sonochemical route," Applied Surface Science Advances, vol. 11, 100304, 2022.

[6] T. Toloshniak, Y. Guhel, J. Bernard, A. Besq, S. Marinel, B. Boudart, "Impact of microwave annealing on CeO_2 thin films sputtered on (111) Si," Materials Research Bulletin, vol. 70, pp. 712-718, 2015.

[7] A. R. Rajan, V. Vilas, A. Rajan, A. John, D. Philip, " Synthesis of nanostructured CeO_2 by chemical and biogenic methods: Optical properties and bioactivity," Ceramic International, vol. 46, pp. 14048-14055, 2020.

[8] A. Corma, "From Microporous to Mesoporous Molecular Sieve Materials

and Their Use in Catalysis," Chemical Reviews, vol. 97, no. 6, pp. 2373-2419, 1997.

[9] M. Aklalouch, A. Calleja, X. Granados, S. Ricart, V. Boffa, F. Ricci, T. Puig, X. Obradors, " Hybrid sol–gel layers containing CeO_2 nanoparticles as UV-protection of plastic lenses for concentrated photovoltaics," Solar Energy Materials and Solar Cells, vol. 120, no. A, pp. 175-182, 2014.

[10] B. Mohanty, A. Chattopadhyay, J. Nayak, " Band gap engineering and enhancement of electrical conductivity in hydrothermally synthesized CeO_2 PbS nanocomposites for solar cell applications," Journal of Alloys and Compounds, vol. 850, 156735, 2021.

[11] S. -Y. Ahn, W. -J. Jang, J. -O. Shim, B. -H. Jeon, H. -S. Roh, "CeO_2-based oxygen storage capacity materials in environmental and energy catalysis for carbon neutrality: Extended application and key catalytic properties," Catalysis Reviews

[12] C. M. Magdalane , K. Kaviyarasu, J. J. Vijaya, B. Siddhardha , B. Jeyaraj, "Facile synthesis of heterostructured cerium oxide/yttrium oxide nanocomposite in UV light induced photocatalytic degradation and catalytic reduction: Synergistic effect of antimicrobial studies," Journal of Photochemistry & Photobiology, B: Biology, vol. 173, pp. 23-34, 2017.

[13] S. Bagheri, I. Khalil, N. M. Julkapli, "Cerium (IV) oxide nanocomposites: Catalytic properties and industrial application," Journal of Rare Earths, vol. 39, no. 2, pp. 129-139, 2021.

[14] A. Umar, T. Almas, A. A. Ibrahim, R. Kumar, M. S. AlAssiri, S. Baskoutas, M. S. Akhtar, “An efficient chemical sensor based on CeO_2 nanoparticles for the detection of acetylacetone chemical,” Journal of Electroanalytical Chemistry, vol. 864, 114089, 2020.

[15] A. Balamurugan, M. Sudha, S. Surendhiran, R. Anandarasu, S. Ravikumar, Y. A. S. Khadar, "Hydrothermal synthesis of samarium (Sm) doped cerium oxide (CeO_2) nanoparticles: Characterization and antibacterial activity," Materials Today: Proceedings, vol. 26, pp. 3588-3594, 2020.

[16] A. S. Fudala, W. M. Salih, F. F. Alkazaz, "Synthesis different sizes of cerium oxide CeO2 nanoparticles by using different concentrations of precursor via sol–gel method," Materials Today: Proceedings, vol. 49, pp. 2786-2792, 2022.

[17] Y. Yulizar, S. Juliyanto, Sudirman, D. O. B. Apriandanu, R. M. Surya, "Novel sol-gel synthesis of CeO_2 nanoparticles using Morinda citrifolia L. fruit extracts: Structural and optical analysis," Journal of Molecular Structure, vol. 1231, 129904, 2021.

[18] Y. Li, X. Wu, W. Wu, K. Wang, L. Qin, S. Liao, Y. Wen, "Synthesis of CeO2 by thermal decomposition of oxalate and kinetics of thermal decomposition of precursor," Journal of Thermal Analysis and Calorimetry, vol. 117, pp. 399-506, 2014.

[19] J. Zheng, Z. Wang, Z. Chen, S. Zuo, "Mechanism of CeO_2 synthesized by thermal decomposition of Ce-MOF and its performance of benzene catalytic combustion," Journal of Rare Earths, vol. 39, pp. 790-796, 2021.

[20] A. I. Y. Tok, F. Y. C. Boey, Z. Dong, X. L. Sun, "Hydrothermal synthesis of CeO_2 nano-particles," Journal of Materials Processing Technology, vol. 190, no. 1–3, pp. 217-222, 2007.

[21] A. Xie, S. Wang, W. Liu, J. Zhang, Y. Yang, J. Han, "Rapid hydrothermal synthesis of CeO_2 nanoparticles with (2 2 0)-dominated surface and its CO catalytic performance," Materials Research Bulletin, vol. 62, pp. 148-152, 2015.

[22] A. A. Kabure, B. S. Shirke, S. R. Mane, K. M. Garadkar, "Microwave-assisted sol-gel synthesis of CeO_2–NiO nanocomposite based NO_2 gas sensor for selective detection at lower operating temperature," Journal of the Indian Chemical Society, vol. 99, no. 3, 2022.

[23] P. H. Ho, M. Ambrosetti, G. Groppi, E. Tronconi, G. Fornasari, A. Vaccari, P. Benito, "Electrodeposition of CeO_2 and Pd-CeO_2 on small pore size metallic foams: Selection of deposition parameters," Catalysis Today, vol. 334, pp. 37-47, 2019.

[24] J. de Souza, A. G. P. da Silva, H. R. Paes Jr, "Synthesis and characterization of CeO_2 thin films deposited by spray pyrolysis," Journal of Materials Science: Materials in Electronics, vol. 18, pp. 591-596, 2007.

[25] S. R. Ardekani, A. S. R. Aghdam, M. Nazari, A. Bayat, E. Yazdani, E. Saievar-Iranizad, "A comprehensive review on ultrasonic spray pyrolysis technique: Mechanism, main parameters and applications in condensed matter," Journal of Analytical and Applied Pyrolysis, vol. 141, 104631, 2019.

[26] L. dos Santos-Gómez, J. Zamudio-García, J. M. Porras-Vázquez, E. R. Losilla, D. Marrero-López, "Highly oriented and fully dense CGO films prepared by spray-pyrolysis and different precursor salts," Journal of the European Ceramic Society, vol. 40, no. 8, pp. 3080-3088, 2020.

[27] J. A. Oke, T. -C. Jen, "Atomic layer deposition and other thin film deposition techniques: From principles to film properties," Journal of Materials Research and Technology, vol. 21, pp. 2481-2514, 2022.

[28] S. R. Sriram, S. R. Parne, N. Pothukanuri, D. R. Edla, "Prospects of spray pyrolysis technique for gas sensor applications – A comprehensive review," Journal of Analytical and Applied Pyrolysis, vol.164, 105527, 2022.

[29] A. B. Workie, H. S. Ningsih, S. - J. Shih, "An comprehensive review on the spray pyrolysis technique: Historical context, operational factors, classifications, and product applications," Journal of Analytical and Applied Pyrolysis, vol. 170, 105915, 2023.

[30] S. Kurtaran, M. Kellegöz, S. Köse, "Characterization of Gd doped CeO_2 thin films grown by ultrasonic spray pyrolysis," Optical Materials, vol. 117, 111144, 2021.

[31] S. Karakaya, L. Kaba, "Enhancing the photocatalytic performance of ZnO: Gd films produced by spray pyrolysis using methylene blue pollutant," Journal of Materials Science: Materials in Electronics, vol. 34, no.16, 1295, 2023.

[32] P. J. King, M. Werner, P. R. Chalker, A. C. Jones, H. C. Aspinall, J. Basca, J. S. Wrench, K. Black, H. O. Davies, P. N. Heys, "Effect of deposition temperature on the properties of CeO_2 films grown by atomic layer deposition," Thin Solid Films, vol. 519, no. 13, pp. 4192-4195, 2011.

[33] B. Elidrissi, M. Addou, A. Outzourhit, M. Regragui, A. Bourgrine, A. Kachouane, "Sprayed CeO_2 thin films for electrochromic applications, prepared by spray pyrolysis," Solar Energy Materials and Solar Cells, vol. 69, no. 1, pp 1-8, 2001.

[34] O. Vigil, F. Cruz, A. M. Acevedo, G. C. Puente, L. Vaillant, G. Santana, "Structural and optical properties of annealed CdO thin films prepared by spray pyrolysis," Material Chemistry and Physics, vol. 68, no. 1-3, pp. 249-252, 2001.

[35] R. G. Solanki, P. Rajaram, P. K. Bajpai, "Growth, characterization and estimation of lattice strain and size in CdS nanoparticles: X-ray peak profile analysis," Indian Journal of Physics, vol. 92, no. 5, pp. 595–603, 2018.

[36] A. Banerji, V. Grover, V. Sathe, S. K. Deb, A. K. Tyagi, "CeO_2-Gd_2O_3 system:

Unraveling of microscopic features by Raman spectroscopy," Solid State Communication, vol. 149, no. 39-40, pp. 1689-1692, 2009.

[37] B. P. Mandal, V. Grover, M. Roy, A. K. Tyagi, "X-ray diffraction and raman spectroscopic investigation on the phase relations in Yb_2O_3- and Tm_2O_3-substituted CeO_2," Journal of American Ceramic Society, vol. 90, no.9, pp. 2961-2965, 2007.

[38] D. N. Durgasri, T. Vinodkumar, P. Sudarsanam, B. M. Reddy, "Nanosized CeO_2–Gd_2O_3 mixed oxides: Study of structural characterization and catalytic CO oxidation activity," Catalysis Letters, vol. 144, pp. 971–979, 2014.

[39] F. Adar, G. leBourdon, J. Reffner, A. Whitley, "FT-IR and Raman Microscopy on a United Platform," Spectroscopy, vol. 18, no. 2, pp. 34–40, 2003.

[40] M. Dronova, V. Lair, P. Vermaut, A. Ringuedé, V. An, "Study of ceria thin films prepared via electrochemical deposition: Role of selected electrochemical parameters on growth kinetics," Thin Solid Films, vol. 693, 137674, 2020.

[41] R. Murugan, G. Vijayaprasath, G. Ravi, "The influence of substrate temperature on the optical and micro structural properties of cerium oxide thin films deposited by RF sputtering," Superlattices and Microstructures, vol. 85, pp. 321–330, 2015.

[42] P. Dorenbos, "Crystal field splitting of lanthanide $4f^{n-1}$ 5d-levels in inorganic compounds," Journal of Alloys and Compounds, vol. 341, no. 1-2, pp. 156–159, 2002.

[43] C. O. Avellaneda, M. A. C. Berton, L. O. S. Bulhoes, "Optical and electrochemical properties of CeO_2 thin film prepared by an alkoxide route," Solar Energy Materials and Solar Cells, vol. 92, no. 2, pp. 240–244, 2008.